Numerical study of secondary mass flow modulation in a Bypass Dual-Throat Nozzle

Numerical Study of Secondary Mass Flow Modulation in a Bypass Dual-Throat Nozzle

M.H. Hamedi-Estakhrsar[a,*], M. Ferlauto[b], H. Mahdavy-Moghaddam[a]

[a]Department of Aerospace Engineering, K.N. Toosi University of Technology, Tehran, Iran

[b]Department of Aerospace and Mechanical Engineering, Politecnico di Torino, Turin, Italy

Abstract

The fluidic thrust-vectoring modulation on a Bypass Dual-Throat Nozzle (BDTN) is studied numerically. The thrust vectoring modulation is obtained by varying the secondary mass flow, introducing different area contraction ratios of the bypass duct. The scope of present study is twofold: (i) to set up a model for the control of the secondary mass flow that is consistent with the resolution of the nozzle main flow and (ii) to derive a simplified representation of a valve system embedded in the bypass channel. The simulations of the turbulent airflow inside the BDTN and its efflux in the external ambient have been simulated by using RANS approach with RNG k-ε turbulence modeling. The numerical results have been validated with experimental and numerical data available in the open literature. The nozzle performance and thrust vector angle are computed for different values of the bypass area contraction ratio. The effects of different secondary mass flow rates on the system resultant thrust ratio and discharge coefficient of the bypass dual-throat nozzle have been investigated. By using the proposed approach to the secondary mass flow modulation, the thrust pitch angle has been controlled up to 27º.

Keywords: Bypass Dual-Throat Nozzle, Fluidic Thrust Vectoring, Supersonic Nozzle, Active Flow Control, Numerical Simulation

*_Corresponding author

Email address: hadihamedi@email.kntu.ac.ir (M. H. Hamedi-Estakhrsar)

1. Introduction

Thrust Vectoring (TV) technologies aim to affect the aircraft (or rocket) dynamics by generating side forces in the nozzle flow. This effect can be achieved either by using deflector devices and movable nozzles [1], or by manipulating and breaking the symmetry on nozzle of fixed geometry [2]. Lateral components of the thrust vector are used for controlling the aircraft dynamics.

Thrust vectoring greatly improves maneuverability, at high angles of attack or at low speeds, for instance, where conventional aerodynamic control surfaces lose effectiveness. Thrust Vector Control is currently achieved by complex arrays of mechanical actuators capable of modifying the geometry of the nozzle and thus enabling to deflect the flow. Different concepts have been developed in the last decade in order to redirect the thrust without mechanical actuators, by active manipulation of the nozzle flow-field. Fluidic Thrust Vectoring (FTV) involves the nozzle flow manipulation by secondary flow injection. AFTV system has the advantage of being lightweight, simple, inexpensive and free from movable parts. Moreover, it can be implemented with the minimum penalty of the aircraft observability [3]. Because of these advantages, several approaches to fluidic thrust-vectoring have been proposed in the past years, including Coanda effect by use of co-flow blowing and counter-flow aspiration [4,5] shock vector control [6-10], throat-skewing [11] and Dual-Throat Nozzle (DTN) configuration [2, 12,13].

Among these, the DTN configuration has shown to achieve greater thrust vectoring efficiency, without compromising the axial component of thrust [2]. The DTN concept has been proposed at NASA LaRC and investigated both computationally and experimentally [2,14]. Both two-dimensional and axisymmetric configurations have been considered. Different area ratios between the first and second throat have been analyzed in order to explore the system performance for different adaptation altitudes or nozzle operation conditions [15]. The effects of an external free stream on thrust vector angle and nozzle performance have been also investigated [16]. By using a numerical framework of the vectored nozzle based on the URANS equations, the dynamic response of the dual-throat nozzle has been investigated in open-loop and closed-loop control [12, 17]. Approaches which are not involved an external source of bleeding air have been also investigated. Active flow control strategies by using the synthetic jets [18] or plasma actuators [19] have been studied.

The simplest way of forcing the flow without any external air source is the use of a bypass duct for feeding the secondary mass flow. The bypass duct connects the nozzle inlet with the target section, e.g. the first throat for the DTN configuration [20], or at a section close to the nozzle outlet, for the shock vector control system [7]. In so doing, the nozzle system does not require any external flow or energy source for generating the secondary flow. A bypass is set from upstream of convergent section to upstream of the first throat of the common DTN [20-22]. The bypass connects the nozzle inlet region, (before the convergent section), with upstream region of the first throat, as shown in Figure 2. The experimental test has shown that the bypass-DTN performance is similar to the classical DTN [20, 22]. Theoretically there are some penalties because of the mass flow spillage from the primary flow. Anyway, it should be noted that the performance described in literature does not take into account the cost of generating the secondary mass flow, since the BDTN does not require any spillage from other engine

components. By a rough comparison we can observe that the BDTN has better performance than the other fluidic thrust vectoring concepts which reported in the literatures.

The works about the bypass dual-throat nozzle focus mainly on the potentiality of this nozzle concept. An analysis on the effect of varying the secondary mass flow has been carried out in Ref. [22] by changing the area section of the full bypass duct. Nevertheless, in actual applications, the typical actuators used for varying the secondary mass flow are based on the valve control systems. These devices introduce additional pressure losses and different flow behaviors of the subsonic and supersonic secondary flow regimes.

In the present work a simple model for the secondary mass flow modulation is presented. A bump with different area contractions is inserted in the middle of the bypass duct. According to the thermodynamic conditions at the bypass inlet and outlet regions, the different flow behaviors are then observed. Scope of the research is the analysis of the coupling of bypass and nozzle operating conditions at different bypass area contraction ratios. The numerical simulations predict both the actual mass flow and pressure losses in the bypass duct, as well as the thrust vectoring performances of the main nozzle. The former information is useful for modeling a bypass valve control system, whereas from the overall performance of the system we may deduce reduced order models of the full nozzle, for instance by system identification [12]. In the next section the nozzle system is described and an adaptation of the definition of the thrust vectoring parameters is discussed. Then the numerical and modeling approach are described. Finally, the numerical results for different bypass area contraction ratios are presented and discussed.

2. BDTN Geometry Description

The reference geometry of the bypass dual-throat nozzle which considered here has been proposed and studied by Gu et al. [20]. Experimental and numerical data are available for this nozzle configuration. A sketch of the nozzle geometry is shown in Figure 1. Some geometrical dimensions and parameters adopted in the baseline of the bypass dual-throat nozzle are given in Table 1. The reader is referred to Ref. [20] for more details. Fine details (e.g. some radius of curvature and the actual throat geometry) was not fully disclosed in Refs. [20, 21, 23] and have been deduced in present work with some approximation by using a plot digitizer. Therefore we expect that some discrepancies may arise in the CFD results.

[Figure 1 about here.]

[Table 1 about here.]

Going further, a modification of the baseline bypass duct has been introduced in order to modulate the secondary mass flow. A portion of the constant duct is replaced by a converging-diverging channel by

introducing a contraction ratio as depicted in Figure 2. The generic point (x,y) on the modified lower wall contour of the bypass channel is expressed as

$$x(\xi)=(1-\xi)x_a+\xi x_b \qquad 0<\xi<1$$
$$y(\xi)=y_a+0.5(h_c-h_t)[1-\cos(2\pi\xi)] \tag{1}$$

[Figure 2 about here.]

Where ξ is a normalized axial coordinate with $[x(0),y(0)]=[x_a,y_a]$ and $[x(1),y(1)]=[x_b,y_b]$. The parameters h_c and h_t are the channel and throat height, respectively.

The value of the height h_c is fixed, whereas h_t may vary in order to obtain different area contraction ratios AR = h_t/h_c. Some bypass wall shapes obtained for different values of the parameter AR are presented in Figure 3.

[Figure 3 about here.]

In a wide sense, the contraction parameter AR represents the amount of opening of a generic valve regulating the bypass flow, with AR = 0 and AR= 1 being the fully-closed and fully-open statuses, respectively. To illustration of the effect of the AR on the nozzle internal flow behavior, the numerical schlieren of the steady flow field at NPR=3 and AR=0.4 has been shown in Figure 4.

[Figure 4 about here.]

3. BDTN Performance Parameters

Thrust-vectoring performance of fluidic vectored nozzle are measured and compared by means specific parameters [1]. These parameters were defined initially by thinking the secondary injection as provided by an external source of bleeding air. In the present case, the secondary flow is extracted from the main nozzle itself by means of the bypass channel. As a consequence, some initial assumptions on what the costs will be and about the concept of primary and secondary flow must be reconsidered. Therefore, we resume the modified typical performance parameters of fluidic thrust vectoring for the BDTN technology. Thrust vectoring techniques are evaluated with some common parameters such as the nozzle discharge coefficient C_d, system resultant thrust ratio C_f, thrust vector angle δ and thrust vectoring efficiency η [2].

Assuming the primary mass flow w_p as the mass flow entering the main nozzle, w_p is then split at the bypass inlet station into two parts, namely w_s and w_n. The fraction of w_s, represent the mass flow which passes inside the bypass channel, and it is also known as 'secondary' mass flow. The fraction of w_n remains inside the main nozzle.

At the bypass exit section, near the first throat of the main nozzle, the two contributions are mixed together. Therefore we have again

$$w_p = w_n + w_s \tag{2}$$

We may also introduce the bypass ratio as

$$\mathrm{BPR} = \frac{w_s}{w_n} \tag{3}$$

The nozzle discharge coefficient C_d is the ratio of the actual nozzle outlet mass flow to the ideal mass flow. In the BDTN case, this coefficient is determined by

$$C_d = \frac{w_n + w_s}{w_{\mathrm{ip}}} = \frac{w_p}{w_{\mathrm{ip}}} \tag{4}$$

The ideal mass flow rate w_{ip} is composed by two contributions as $w_{ip} = w_{in} + w_{is}$.
These contributions are computed according to the one-dimensional isentropic flow theory as

$$\begin{aligned} w_{\mathrm{in}} &= \frac{P_0 A_t}{\sqrt{\mathrm{RT}_0}} \sqrt{\gamma} \left(\frac{2}{\gamma+1} \right)^{\frac{\gamma+1}{2(\gamma-1)}} \\ w_{\mathrm{is}} &= \frac{P_0 A_{\mathrm{t,s}}}{\sqrt{\mathrm{RT}_0}} \sqrt{\gamma} \left(\frac{2}{\gamma+1} \right)^{\frac{\gamma+1}{2(\gamma-1)}} \end{aligned} \tag{5}$$

As usual, the parameter of γ is the specific heat ratio and R is the gas constant. The parameter of A_t is the nozzle throat area of R. Gu et al. [20] experimentally tested geometry and $A_{t,s}$ is the throat area of the bypass duct. The discharge coefficient has been defined by dividing the actual mass flow rate to the ideal mass flow rate which can be passed from the experimentally tested geometry.

In a similar fashion, a bypass discharge coefficient C_{db} can be introduced as

$$C_{\mathrm{db}} = \frac{w_s}{w_{\mathrm{is}}} \tag{6}$$

Which is a measure of the actual mass flow evolving in the bypass duct with respect to the ideal one w_{is}. The w_{is}, can be computed exactly. The throat area of the bypass duct and the total conditions P_0 and T_0 of the bypass entry are known. In a lower order model of the bypass device, the parameter C_{db} can be interpreted as the correction factor required for deriving a reliable estimation of the actual mass flow from the analytical isentropic solution.
The nozzle we are dealing with is very uncommon and the classical findings for standard nozzle are more difficult to be applied. For this reason some parameters have sense and can be analytically computed

under some assumptions or flow regime only. For w_{in}, the only assumption we can made is $A_{min}=A_t$ (and this has been done also by the experimentalists who tested the nozzle) and to consider the choked case only. It did not make sense for w_{is} a different definition, so that C_{db} has been normalized with respect to the choked condition too. Without loss of generality, by using C_{db}, the working conditions of the bypass duct have been modelled with details both in the choked and un-chocked case and an analytical model have been formulated in section. For this reason, we computed the discharge coefficient C_{db} as a function of the bypass duct working conditions and contraction ratio AR.

The system resultant thrust ratio C_f is defined as the ratio between the modulus of the thrust obtained and the ideal thrust that the primary and secondary mass flow can generate at the same discharge pressure P_e. According to the BDTN system, we set

$$C_f = \frac{\sqrt{F_{A^2} + F_{N^2}}}{F_{\text{in}} + F_{\text{is}}} \tag{7}$$

Where F_A and F_N represent the axial and normal force components, respectively. The ideal thrust contributions are computed as

$$\begin{aligned} F_{\text{in}} &= w_n \sqrt{\frac{2\gamma \text{RT}_0}{\gamma - 1}\left[1 - \left(\frac{P_e}{P_0}\right)^{\frac{\gamma-1}{\gamma}}\right]} \\ F_{\text{is}} &= w_s \sqrt{\frac{2\gamma \text{RT}_0}{\gamma - 1}\left[1 - \left(\frac{P_e}{P_0}\right)^{\frac{\gamma-1}{\gamma}}\right]} \end{aligned} \tag{8}$$

The thrust deflection angle is then

$$\delta = \tan^{-1}\left(\frac{F_N}{F_A}\right) \tag{9}$$

Finally, remembering that the conventional cost of the FTV is the percentage of secondary air mass flow spent in actively controlling the flow instead of producing thrust, we introduce the mass flow ratio MFR as

$$\text{MFR} = \frac{w_s}{w_n + w_s} = \frac{w_s}{w_p} = \frac{\text{BPR}}{\text{BPR} + 1} \tag{10}$$

The thrust-vectoring efficiency is then deduced

$$\eta = \frac{\delta}{100\text{MFR}} = \frac{\delta(\text{BPR} + 1)}{100(\text{BPR})} \tag{11}$$

Where δ is conventionally measured in degrees.

4. Numerical Method

4.1. Flow Governing Equations

The fluid flow is governed by the compressible Reynolds Averaged Navier-Stokes equations (RANS) coupled to the RNG k-ε turbulence model. The simulations have been carried out by using the CFD package Ansys Fluent R19.2, which is based on a finite-volume discretization of the flow governing equations.

Several numerical investigations about nozzle flows have pointed out that turbulence modeling has a strong impact in the correct capture of the shock-boundary layer interactions [12, 24, 26]. In particular, the use of wall-functions can lead to an incorrect prediction of the unsteady separation points. The full resolution of the boundary layers, without using wall-functions, even with a simpler one-equation model of turbulence must be preferred. Anyway, in many simulations of the dual-throat nozzle [2, 20, 23, 27 and 28] the RNG k-ε turbulence model with standard wall functions has been adopted. The obtained results were in good agreement with the related experimental data. Therefore, we adopted the same approach to turbulence modeling and checked some of the solutions by using the Spalart-Allmaras turbulence model without wall functions [12].

Briefly, the system of the governing equations can be described as follows

$$\frac{\partial \rho}{\partial t}+\frac{\partial}{\partial x_i}\left(\rho u_i\right)=0 \tag{12}$$

$$\frac{\partial}{\partial t}\left(\rho u_i\right)+\frac{\partial}{\partial x_j}\left(\rho u_i u_j\right)=\frac{-\partial p}{\partial x_i}+\frac{\partial}{\partial x_j}\left[\mu\left(\frac{\partial u_i}{\partial x_j}+\frac{\partial u_j}{\partial x_i}-\frac{2}{3}\delta_{\mathrm{ij}}\frac{\partial u_k}{\partial x_k}\right)\right]+\frac{\partial}{\partial x_j}\left(-\rho\overline{u_i^{'}u_j^{'}}\right) \tag{13}$$

$$\frac{\partial}{\partial t}\left(\rho E\right)+\frac{\partial}{\partial x_i}\left[u_i\left(\rho E+p\right)\right]=\frac{\partial}{\partial x_j}\left[\left(k+\frac{C_p\mu_t}{P_{\mathrm{rt}}}\right)+u_i\left(-\rho\overline{u_i^{'}u_j^{'}}\right)\right] \tag{14}$$

Which express mass, momentum and energy balance, respectively. As usual, ρ is density, p is pressure, μ is viscosity. Terms as u denote mean quantities, whereas u' is a fluctuating quantity. The terms $\left(-\rho\acute{u}_i\acute{u}_j\right)$ are the Reynolds stress tensor. This set of equations require a turbulence closure model, i.e. the RNG k-ε model [29] in our case.

The transport equations of the above mentioned model are

$$\frac{\partial}{\partial t}\left(\rho k\right)+\frac{\partial}{\partial x_i}\left(\rho\,\mathrm{k}u_i\right)=\frac{\partial}{\partial x_i}\left(\alpha_k\mu\frac{\partial k}{\partial x_j}\right)+G_k+G_b-\rho\varepsilon-Y_M+S_k \tag{15}$$

And

$$\frac{\partial}{\partial t}\left(\rho\varepsilon\right)+\frac{\partial}{\partial x_i}\left(\rho\varepsilon u_i\right)=\frac{\partial}{\partial x_i}\left(\alpha_\varepsilon\mu\frac{\partial \varepsilon}{\partial x_j}\right)+C_{1e}\frac{\varepsilon}{k}\left(G_k+C_{3\varepsilon}G_b\right)-C_{2\varepsilon}\rho\frac{\varepsilon^2}{k}-R_\varepsilon+S_\varepsilon \tag{16}$$

Where G_k and G_b represent the generation of turbulence kinetic energy due to the mean velocity gradients and to buoyancy, respectively. Y_M is the contribution of the fluctuating dilatation to the overall dissipation rate. The quantities α_k and α_ε are the inverse effective Prandtl numbers for k and ε, respectively. S_k and S_ε are user-defined source terms. Turbulent viscosity is defined as

$$\mu_t = \rho C_\mu \frac{k^2}{\varepsilon} \tag{17}$$

With $C\mu = 0.0845$.

4.2. Boundary conditions

The adopted boundary conditions are dependent on the solver, but in all cases they are an expression of the hyperbolic system of the compressible RANS equations [30]. The adopted boundary conditions are resumed in Figure 5 at each edge of the computational domain.

[Figure 5 about here.]

Briefly, from the general numerical treatment of the boundary conditions for hyperbolic systems, the total temperature, total pressure and the flow direction are imposed at the nozzle inlet. The nozzle flow is discharging in an ambient with calm air. For this condition, an adequate choice is the enforcement of the ambient static pressure at the domain outlet, if the flow is subsonic, whereas no boundary conditions are needed if the flow is supersonic. In latter case, the flow state at boundary is extrapolated from the domain interior. Another suitable, and more stable choice is the enforcement of a non-reflecting boundary condition. Following ANSYS Fluent nomenclature, the Pressure Outlet is set to the downstream boundary condition, whereas the boundaries which discharge to ambient region are simulated by using the Pressure Far-filed condition, as shown in Figure 5. The ambient pressure level is selected according to the nozzle pressure ratios of the testing conditions in Ref. [20]. Finally, the walls are considered as adiabatic, coupled to a no-slip condition for the velocity.

4.3. Grid Sensitivity Study

The independence of the computed flow-fields from the grid size has been checked by comparing the obtained solutions using different meshes. Three different grids have been generated: a coarse mesh (grid A) with a core block mesh of 160×60 quadrilateral cells; a medium mesh (grid B) with 240×120 core block and a finer mesh (grid C) with 360×180 core block, with total number of about 25,000 , 50,000 and 100,000 cells, respectively. The computational mesh B with finer details near the nozzle throat is shown

in Figure 6. Grid stretching has been introduced in order to reach a minimum $y^+ = 5$ along the nozzle to meet the requirements of the RNG k-ε turbulence model and standard wall function.

[Figure 6 about here.]

In order to obtain independent domain, the downstream of the nozzle exit was extended by 40 times the outlet height along x-direction and 16 times along the y-direction.

Figure 7 shows the predicted pressure distributions at NPR=3 on the top and bottom walls of the nozzle (starting from the first throat section) by using the three different grids. It can be seen that a grid independent solution is obtained by Grid B that has been therefore selected as reference grid in the computations of the nozzle performances throughout the work. Different values of the contraction ratio AR modify the grid locally, in the bypass duct.

[Figure 7 about here.]

4.4. Numerical Validation

Alongside the grid sensitivity study, the computational results of the original BDTN configuration have been compared with the numerical and experimental data available in Gu et al. [20]. This configuration corresponds to our case with AR=1.

The pressure distributions on the upper and lower wall of the nozzle at NPR=3 are shown in Figure 8. The agreement between present numerical results and results of Ref. [20] is very good. The main differences rely on the shock position in the bottom wall. In other parts of the nozzle, present numerical simulation are even closer than [20] to the experimental data [20]. With the aim of checking if the mismatch is related to the discretization schemes, we computed the solution by using two different solver available in Ansys Fluent for compressible flow, namely solver A and solver B. The first is a pressure-based solver with energy coupling [31], whereas the latter is a density based solver.

[Figure 8 about here.]

The RNG k-ε turbulence model has been used in both cases, as mentioned in previous sections. The two solutions, plotted in Figure 8, are almost identical.

The experimental data does not give any further insight, since they are matched more or less with the same accuracy by all three numerical solutions. Moreover, the use of other turbulence models, e.g. Spalart-Allmaras one equation model, did not improve the solution. We concluded that this behavior

depends on a possible mismatch between the geometry we deduced by using a plot digitizer from the original Ref. [20] in the first throat region.

A second analysis has been carried out by comparing the nozzle performances at different NPRs computed by present method with the results in [20]. The plots for the thrust angle δ and system resultant thrust ratio C_f are shown in Figure 9.

[Figure 9 about here.]

The results show that the present work predictions underestimate δ and C_f of about 3.7% and 2.2%, respectively. But the value of these differences is the same and is in the reasonable range. By increasing the nozzle pressure ratio from NPR=3 to NPR=5 the maximum thrust angle reduces from δ= 27° to 21°.

5. Secondary Mass Flow Modulation

In this section the effects of the secondary mass flow modulation on the BDTN performance are discussed. The mass flow modulation is obtained here by modifying the area distribution of a portion only of the bypass duct. The effects of the secondary mass flow on the thrust vectoring performance parameters of dual throat nozzles have been addressed in many experimental and numerical investigations [2, 27]. Also experimental data about the nozzle dynamics for the BDTN configuration are available [21]. The mass flow modulation has been obtained by changing the bypass channel height h_c for axisymmetric BDTN geometry [22]. In the present approach, we control the bypass mass flow rate by a local variation of the bypass geometry by using a contraction duct with minimal height h_t. Therefore, the main purpose of this study is to determine the relationship between the bleeding mass flow rate and the bypass outlet condition by using the prescribed area contraction ratio AR.

5.1. About the coupling of main nozzle and bypass duct

Focusing on the dynamics of the system as a whole, we need to understand how the main nozzle and the bypass duct interact with each other. The main nozzle is a converging-diverging-converging nozzle where the flow is accelerated up to supersonic conditions. The flow reaches the sonic conditions in the neighborhood of the first throat, which is also the region where the bypass outlet is located. Basically, the flow path inside the main nozzle is very similar to the pure dual-throat nozzle [2, 27]. Experimental and numerical investigations have revealed that the flow field inside the DTN is dominated by the two standing vortices trapped in the upper and lower cavities between the two throats. The unsteady flow field is dominated by dynamics of these vortex structures, which is also able to modify the shock pattern and

position. At the steady state, the vortex location is triggered by the fixed separations generated by the secondary air injection [12, 32].

The BDTN concept just replaces the external source of bleeding air by the bypass flow. Although a stronger coupling between the two components is expected, the flow perturbations generated by the bypass flow inside the main nozzle remain qualitatively comparable to that generated by the secondary air in the pure DTN case [23].

The involved physical scenario is illustrated in Figure 10, where the flow fields are represented different AR values in terms of the Mach number contour maps.

[Figure 10 about here.]

The interaction zone between the bypass duct and the main nozzle can be identified clearly in the region of the nozzle first throat. As visible in Figure10, this region remains close to sonic conditions in every case. Qualitatively, we can observe that the higher AR leads to the higher the secondary mass flow. This fact leads in turn to a higher shift of the sonic line towards the main nozzle outlet when AR is increasing. As a consequence, the static pressure at the bypass outlet remains a little bit higher than the critical one every time. The higher secondary mass flow (the higher sonic line shift in the main nozzle) leads to the higher pressure at the interaction zone between the two devices. At the bypass inlet, instead, the flow conditions are very close to that at the main nozzle inlet, if we neglect the effects of the boundary layer developing on the upper wall of the main nozzle.

This assumption is also supported by the distribution of the losses inside the flow field. Contour maps of the total pressure loss $\Delta P_o/P_o$ for different area contraction ratios AR of the bypass duct are illustrated in Figure 11. This figure also gives useful insights on the regions where the major part of the losses is generated.

[Figure 11 about here.]

5.2. Bypass duct performances

Thought the general system dynamics being driven by the main nozzle flow field, as discussed in previous section, we now analyze the operating conditions of the bypass duct for different contraction area ratios AR. The results of working conditions are deduced from the CFD simulation of the complete flow field inside and outside the BDTN. Theoretical considerations about the bypass duct operating conditions are based on the isentropic nozzle flow theory.

As a first step, in order to define the bypass duct working conditions, the area averaged value of the static pressure at the bypass outlet has been extracted from the CFD computations. The obtained pressure levels for different values of AR and NPR are summarized in Figure 12(a).

[Figure 12 about here.]

The theoretical value of the pressure level P_{l1} that generates choked conditions at the bypass throat is displayed in the same plot. As well known, in a nozzle, for a given AR it is possible to identify two exit pressure levels, namely P_{l1} and P_{l2} that allow for an isentropic solution up to a subsonic and supersonic exit flow, respectively. These values are computed by imposing isentropic conditions and continuity $\dot{m}_e = \dot{m}_t$ between the exit section '*e*' and the throat section '*t*' of the bypass duct. It follows

$$F(M_e) = \frac{A_t}{A_e} F(1) = \mathrm{AR}.\sqrt{\gamma}\left(\frac{2}{\gamma+1}\right)^{\frac{\gamma+1}{2(\gamma-1)}} \tag{18}$$

Being also $A_t/A_e = h_t/h_e$ and with

$$F(M) = \frac{\sqrt{\gamma}\, M}{\left(1+\frac{\gamma-1}{2}M^2\right)^{\frac{\gamma+1}{2(\gamma-1)}}} \tag{19}$$

For a given value of AR, by inverting eq. (17) we lead to two solutions $M_{e1} < 1$ and $M_{e2} > 1$ and then to P_{l1} and P_{l2} by imposing that the total pressure is preserved along the duct. Theoretically, if the exit pressure is below $P_e < P_{l1}$, the flow inside the duct should become choked. In the real case the pressure losses along the bypass duct may modify this condition. Another source of approximation is due to the pressure averaging process. The static pressure in the interaction zone between bypass and main nozzle varies very rapidly in space, ranging from values as $(P_w/P_o) = 0.8$ to $(P_w/P_o) = 0.45$, as visible in Figure 8(b), so that an averaged value can become poorly representative of the actual flow conditions. The actual cases in which the duct flow is choked have been reported with filled symbols in Figure 12(a). They correspond to the lower computed ARs values. Alternatively, the chocked flow condition of the bypass could be also deduced from the Mach number iso-contours in Figure 10.

The graphical correlation between the area ratio AR and the secondary mass flow is presented in Figure 12(b). As usual the secondary mass flow is expressed as a fraction of the nozzle mass flow, that is, $MFR = w_s/(w_s + w_p)$. By changing AR in the range of 0.1-1, the secondary mass flow rises from the 1% up to 9%. The behavior is almost linear up to AR = 0.4. In fact close to the choking conditions we have

$$w_s \simeq \left(P_0/\sqrt{\mathrm{RT}_0}\right) F(1) A_e.\mathrm{AR} \tag{20}$$

By considering that $w_p \gg w_s$ this results also in a linear relationship between MFR and AR.

In view of the development of an analytical model [33] for the bypass duct, it could be useful the derivation of a parameter similar to the discharge coefficient of the main nozzle. That parameter has been defined as C_{db} in eq. (5). The graphical representation of the parameter is shown in Figure 12(c). Its knowledge allow us to derive an estimation of the actual flow in the bypass duct from the theoretical value. Moreover, realistic valve-based systems could be modeled by recalibrating this basic function in order to better match actual bypass performances.

5.3. Overall thrust-vectoring performances

Finally, in this section the overall performance of the nozzle system under different thrust-vectoring settings is discussed. The diagrams in Figure 13 illustrate the nozzle system performance in terms of the usual thrust-vectoring parameters C_d, C_f, δ, η. Although the bypass dual-throat nozzle is a variant of the dual-throat nozzle, the operating conditions have different ranges of variation.

[Figure 13 about here.]

For instance, in the present case the MFR varies up to the 9%, which is twice that of the DTN tested at NASA LaRC [27] but similar, anyway, to the values of other BDTNs [22].

Unfortunately we are unable to make comparison with experimental data, since data available in literature for present configuration refers mainly to wall pressure distribution under the steady state or unsteady response. The global performance parameters are not reported [20, 21]. Nevertheless, such parameters are a direct expression of the pressure distributions and of the primary/secondary mass flow that we have compared already.

As a common behavior of all diagrams in Figure 13 (except the thrust vectoring efficiency η) a linear trend with MFR can be observed for MFR > 3% .The secondary mass flow ratio MFR = 3% is reached at $AR \cong 0.2$.

As show in Figure 13(a), the discharge coefficient C_d is ranging from 0.91 to 0.98 and it is almost linear with MFR. The NPR seems to have a weak influence, since the two curves are very close.

In the same range of MFR, the system resultant thrust ratio C_f is nearly constant. The value is very close to that obtained by a DTN at similar conditions and nozzle pressure ratios [27].

A remarkable feature of the BDTN tested, either numerically or experimentally, is reached the high thrust angle. We obtained values up to δ_{max} = 20º-30º. Moreover, by comparing the available data [14] at similar values of MFR and NPR, the obtained thrust vectoring efficiency η remains in the same range of the DTN case, (at about 4-5 degrees/%MFR)

Alongside the usual parameters for evaluating the nozzle vectoring performance, we present the diagrams of the axial F_A and normal F_N nozzle force components, respectively. These parameters, normalized with the ideal force F_{ip}, are shown in Figure 13 (e and f). These curves are all monotonic and increasing with MFR, as shown in Figures 13(e and f). Therefore we can argue that the higher thrust angles are actually due to a relative increase of F_N rather than caused by a decrease of the axial thrust component F_A.

Finally, note that the diagrams of Figure 13 do not only resume the performance parameters of the system under study, but also they may express a self-contained reduced order model of the whole nozzle system. Once the value of MFR is deduced from Figure 12(b), all the other information obtains from the plots in Figure 13. This approach is supposed to be general enough to still hold when the bypass performance parameters MFR(AR) and C_{db}(AR) are replaced by empirical formulations extracted from other valve models.

6. Acknowledgments

The financial support by the Ministry of Science, Research and Technology of Iran and by the Politecnico di Torino is gratefully acknowledged by the first author.

7. Conflicts of interest.

There are no conflict of interests to declare.

8. Conclusions

In the present work the controllability of the bypass dual-throat nozzle has been investigated numerically. The flow inside the BDTN as well as the evolution of nozzle jet flow in the discharge ambient are simulated by CFD. The analysis focused on the interactions between the flow inside the main dual-throat nozzle and in the bypass duct. The latter is providing the secondary mass flow injection required for fluidic thrust vectoring. A simple mechanism of secondary mass flow modulation has been introduced by varying the area distribution in a fixed portion of the bypass duct. The model retains the fundamental aspects of fluid dynamic modeling of a valve. The results can be calibrated on experimental data of a specific valve configuration.

The study of the interaction between the bypass duct and the main nozzle has been divided into two parts. First the effect of the bypass area contraction ratio AR was studied on the flow rate w_s and on the losses. The operating conditions of the bypass duct were also highlighted in relation with the upstream and

downstream averaged pressures. The latter is however a result of the mutual interaction of the two devices.

In the second stage, the effect of secondary mass flow on the thrust vectoring performance of the BDTN was analyzed for different bypass settings and nozzle pressure ratios. A discharge coefficient C_{db} for the bypass duct has been introduced in order to correlate the ideal and the effective mass flow rates in the bypass duct. This parameter should be useful in the modeling a control system embedded in the bypass duct, as well as in the derivation of models of bypass blowing based on user defined boundary conditions or analytical models.

Nomenclature

AR	Area contraction ratio of the bypass duct, h_t/h_c
A_t	Throat area of primary nozzle
$A_{t,s}$	Throat area of bypass duct
BPR	bypass ratio, w_s/w_n
C_d	Nozzle discharge coefficient
C_{db}	Bypass discharge coefficient
C_f	System resultant thrust ratio
F_A	Axial force
F_i	Ideal force
F_N	Normal force
h_c	Bypass channel height
h_t	Bypass channel throat height
MFR	Mass Flow Ratio, w_s/w_p
NPR	Nozzle Pressure Ratio,
w_i	Ideal mass flow
w_n	Nozzle internal mass flow
w_p	Primary mass flow
w_s	Secondary mass flow
δ	Thrust vector angle, $\tan^{-1}(F_N/F_A)$
η	Thrust vectoring efficiency

References

[1] S. Asbury, F. Capone, High-alpha vectoring characteristics of the f-18/harv, Journal of Propulsion and Power, 10 (1) (1994) 116-121.

[2] K. Deere, Summary of fluidic thrust vectoring research conducted at NASA Langley research center, 21st AIAA Applied Aerodynamics Conference, Orlando, Florida, AIAA Paper 2003-3800 (2003) .

[3] M. Mason, W. Crowther, Fluidic thrust vectoring for low observable air vehicles, 2nd AIAA Flow Control Conference, Portland, OR. AIAA paper 2004-2210 (2004).

[4] K. Heo, J.Y.and Yoo, H. Lee, Y. an Sung, Fluidic thrust vector control of supersonic jet using co-flow injection, 45th Joint Propulsion Conference and Exhibit, Colorado (2009) .

[5] K. Kexin Wu, H. Kim, Y. Jin, Fluidic thrust vector control based on counter-flow concept, Proc. IMechE, Part G: Journal of Aerospace Engineering, 233 (4) (2019) 1412-1422.

[6] K. Waithe, K. Deere, An experimental and computational investigation of multiple injection ports in a convergent-divergent nozzle for fluidic thrust vectoring, 21st AIAA Applied Aerodynamics Conference, AIAA paper 2003-3802 (2003).
[7] R. Deng, H. Kim, A study on the thrust vector control using a bypass flow passage, Proc. IMechE, Part G: Journal of Aerospace Engineering 229 (9) (2015) 1722-1729.
[8] S. Eilers, M. Wilson, S. Whitmore, Z. Peterson, Side force amplification on an aerodynamically thrust vectored aero spike nozzle, journal of Propulsion and Power 28 (4) (2012) 811-819.
[9] H. V. Pelt, A. J. Neely, J. Young, A system study on fluidic thrust vectoring, 20th AIAA International Space Planes and Hypersonic Systems and Technologies Conference, Glasgow, UK (2015) .
[10] L. Li, M. Hirota, K. Ouchi, T. Saito, Evaluation of fluidic thrust vectoring nozzle via thrust pitching angle and thrust pitching moment, Shock Waves 27 (1) (2017) 53-61.
[11] P. Yagle, D. Miller, K. Ginn, J. Hamstra, Demonstration of fluidic throat skewing for thrust vectoring in structurally fixed nozzles, ASME Journal of Engineering for Gas Turbines and Power 123 (3) (2001) 502-507.
[12] M. Ferlauto, R. Marsilio, Numerical investigation of the dynamic characteristics of a dual-throat nozzle for fluidic thrust-vectoring, AIAA Journal 55 (1) (2017) 86-98.
[13] C. Shin, H. Kim, T. Setoguchi, S. Matsuo, A computational study of thrust vectoring control using dual throat nozzle, Journal of Thermal Science 19 (6) (2010) 486-490.
[14] J. Flamm, K. Deere, M. Mason, B. Berrier, S. Johnson, Experimental study of an axisymmetric dual throat fluidic thrust vectoring nozzle for a supersonic aircraft application, 43rd AIAA/ASME/SAE/ASEE Joint Propulsion Conference & Exhibit, AIAA paper 2007-5084 (2007) .
[15] M.H. Hamedi Estakhrsar, H. Mahdavy-Moghaddam, M. Jahromi, Investigation of effects of convergence and divergence half-angles on the performance of a nozzle for different operating conditions, Journal of the Brazilian Society of Mechanical Sciences and Engineering 40 (2018) 353-362.
[16] M. Ferlauto, R. Marsilio, Influence of the external flow conditions to the jet-vectoring performances of a SVC nozzle, 55th AIAA/SAE/ASEE Joint Propulsion Conference, Indianapolis, AIAA Paper 1-10 (2019).
[17] M. Ferlauto, R. Marsilio, Open and closed-loop responses of a dual throat nozzle during thrust vectoring, 52nd AIAA/SAE/ASEE Joint Propulsion Conference, Salt Lake City, UT, AIAA Paper 4504 (2016).
[18] M. Ferlauto, Active flow control in supersonic nozzles, AIP Conference Proceedings 1978 (1) (2018) 470035.
[19] M. Abdollahzadeh, F. Rodrigues, J. Pascoa, P. Oliveira, Numerical design and analysis of a multi-dbd actuator configuration for the experimental testing of acheon nozzle model, Aerospace Science and Technology 41 (2015) 259-273.
[20] R. Gu, J. Xu, S. Guo, Experimental and numerical investigations of a bypass dual throat nozzle, ASME Journal of Engineering for Gas Turbines and Power 136 (2014) 084501-1.
[21] R. Gu, J. Xu, Dynamic experimental investigations of a bypass dual throat nozzle, ASME Journal of Engineering for Gas Turbines and Power 137 (8) (2015) 084501.
[22] Y. Wang, J. Xu, S. Huang, Y. Lin, J. Jiang, computational study of axisymmetric divergent bypass dual throat nozzle, Aerospace Science and Technology 86 (2019) 177-190.
[23] R. Gu, J. Xu, Effects of cavity on the performance of dual throat nozzle during the thrust-vectoring starting process, ASME Journal of Engineering for Gas Turbines and Power 136 (1) (2014) 014502.

[24] C. Tian, Y. Lu, Turbulence models of separated flow in shock wave thrust vector nozzle, Engineering Applications of Computational Fluid Mechanics 7 (2) (2013) 182-192.
[25] A. Chaudhuri, A. Hadjadj, Numerical investigations of transient nozzle flow separation, Aerospace Science and Technology 53 (2016) 10-21.
[26] Y. Allamaprabhu, B. Raghunandan, J. Morinigo, Numerical prediction of nozzle flow separation: Issue of turbulence modeling, Aerospace Science and Technology 50 (2016) 31-43.
[27] J. Flamm, K. Deere, M. Mason, B. Berrier, S. Johnson, Design enhancements of the two dimensional, dual throat fluidic thrust vectoring nozzle concept, 3rd AIAA Flow Control Conference, San Francisco, CA, United States, AIAA Paper 2006-3701 (2006) .
[28] K. A. Deere, J. D. Flamm, B. L. Berrier, S. K. Johnson, Computational Study of an Axisymmetric Dual Throat Fluidic Thrust Vectoring Nozzle Concept for Supersonic Aircraft Application. AIAA Paper 2007-5085 (2007).
[29] C. Speziale, S. Thangam, Analysis of a RNG based turbulence model for separated flows, Nasa CR-189600 (1992).
[30] T. Poinsot, S. Lele, Boundary conditions for direct simulations of compressible viscous reacting flows, Journal of Computational Physics 101 (1992) 104-129.
[31] F. Menter, P. Galpin, T. Esch, M. Kuntz, C. Berner, Cfd simulations of aerodynamics flows with a pressure-based method, 24th international Congress of aeronautical Sciences (ICAS2004) (2004) .
[32] A. Elcrat, M. Ferlauto, L. Zannetti, Point vortex model for asymmetric inviscid wakes past bluff bodies, Fluid Dynamics Research 46 (3) (2014) 031407.
[33] B. Maicke, G. Bondarev, Quasi-one-dimensional modeling of pressure effects in supersonic nozzles, Aerospace Science and Technology 70 (2017) 161-169.

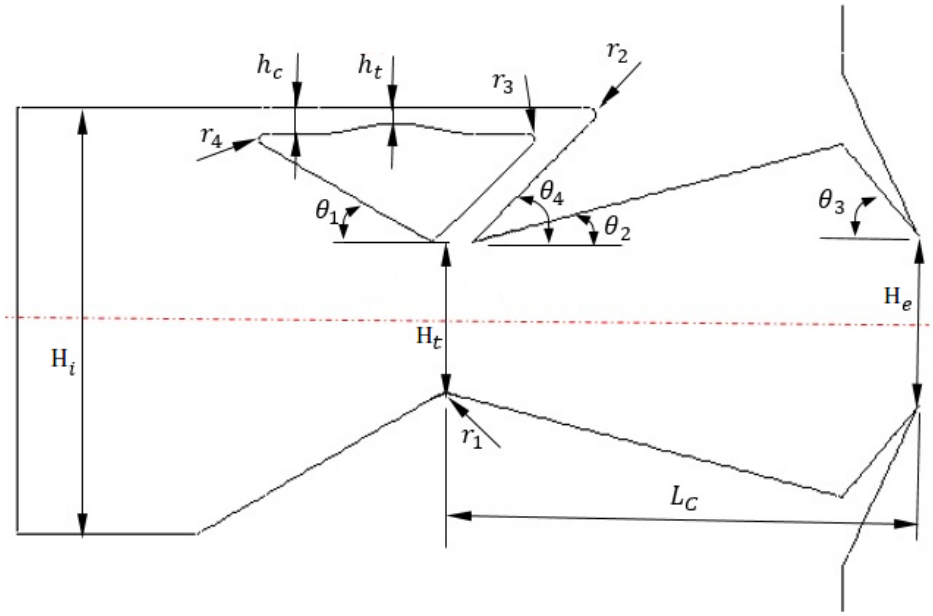

Figure 1. Bypass Dual Throat Nozzle geometry and parameters

180x119mm (96 x 96 DPI)

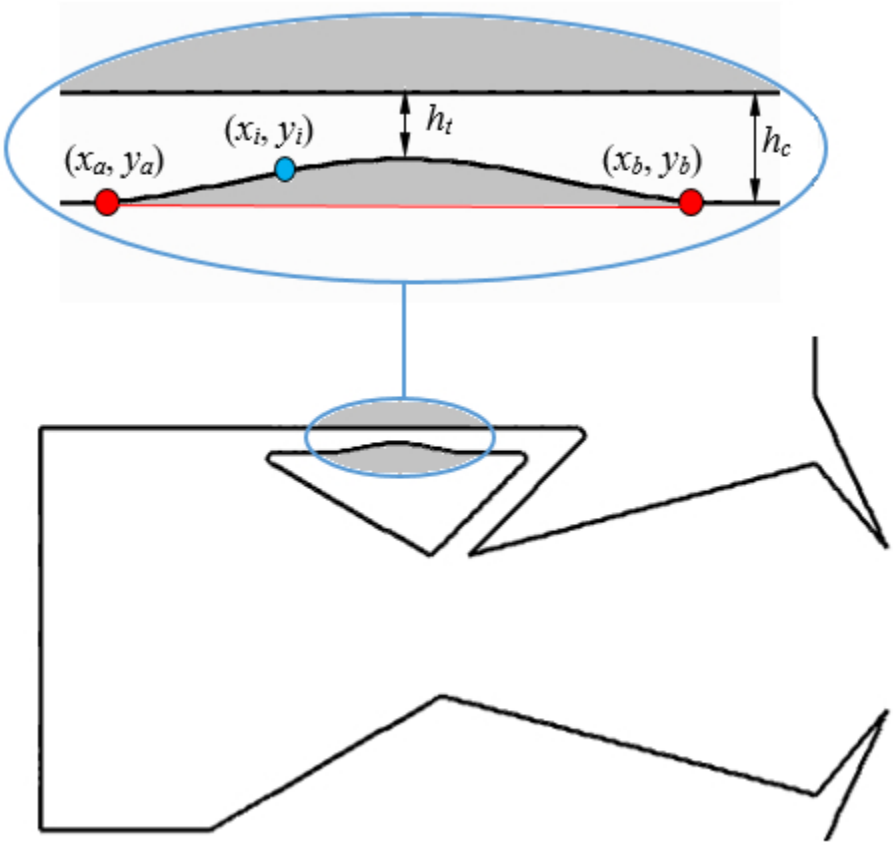

Figure 2. Geometric parameters of the bypass passage contraction

124x122mm (96 x 96 DPI)

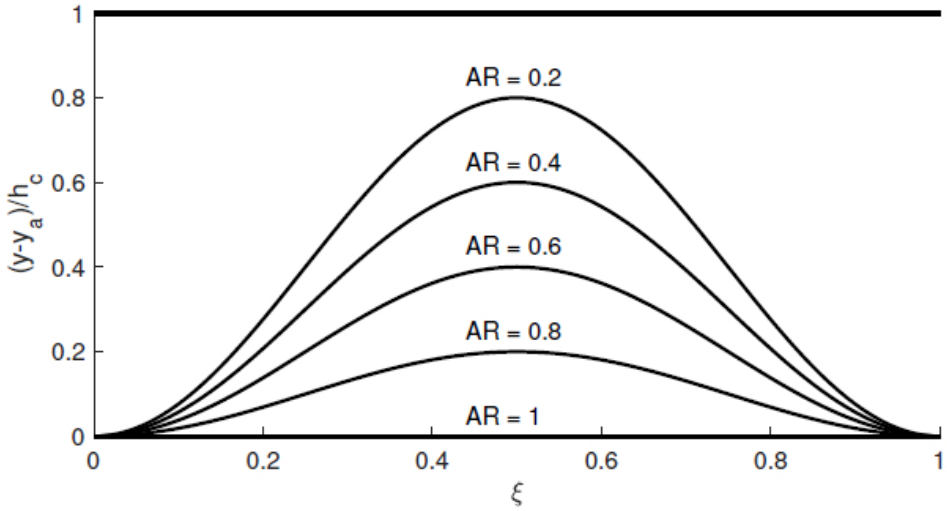

Figure 3. Bypass contour for different values of the area contraction ratio AR

168x93mm (96 x 96 DPI)

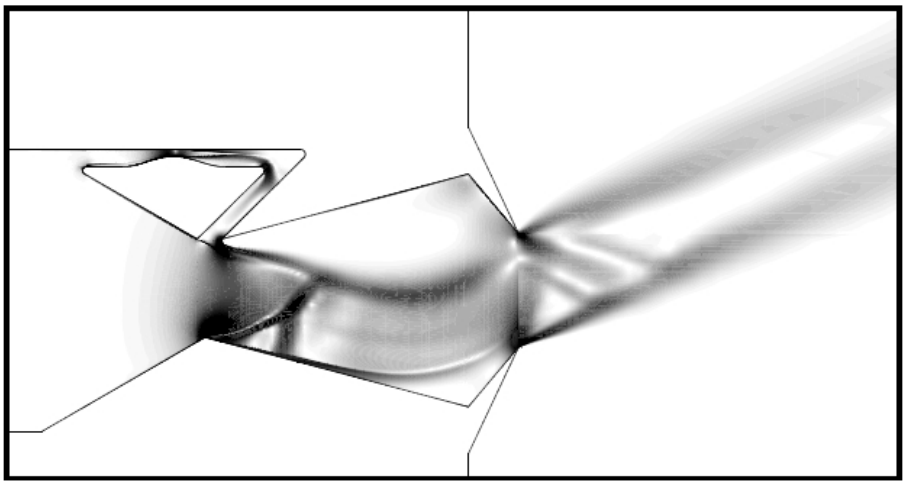

Figure 4. Numerical schlieren of the steady flow field (NPR=3, AR=0.4)

182x100mm (96 x 96 DPI)

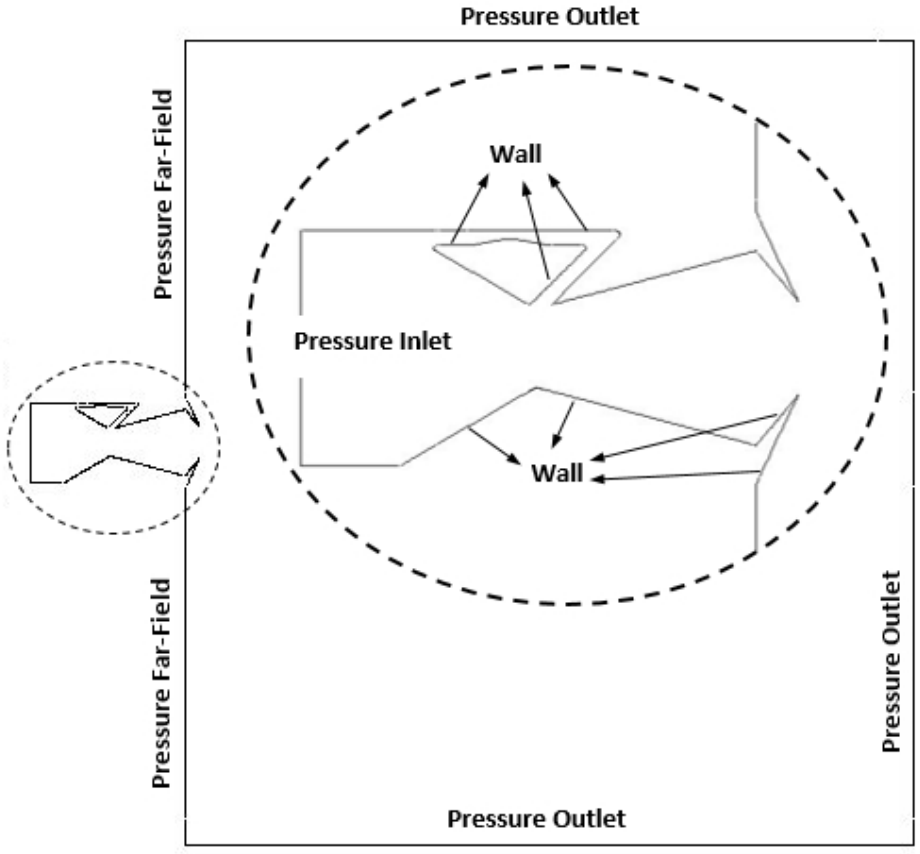

Figure 5. Sketch of the boundary conditions imposed on the computational domain

140x130mm (96 x 96 DPI)

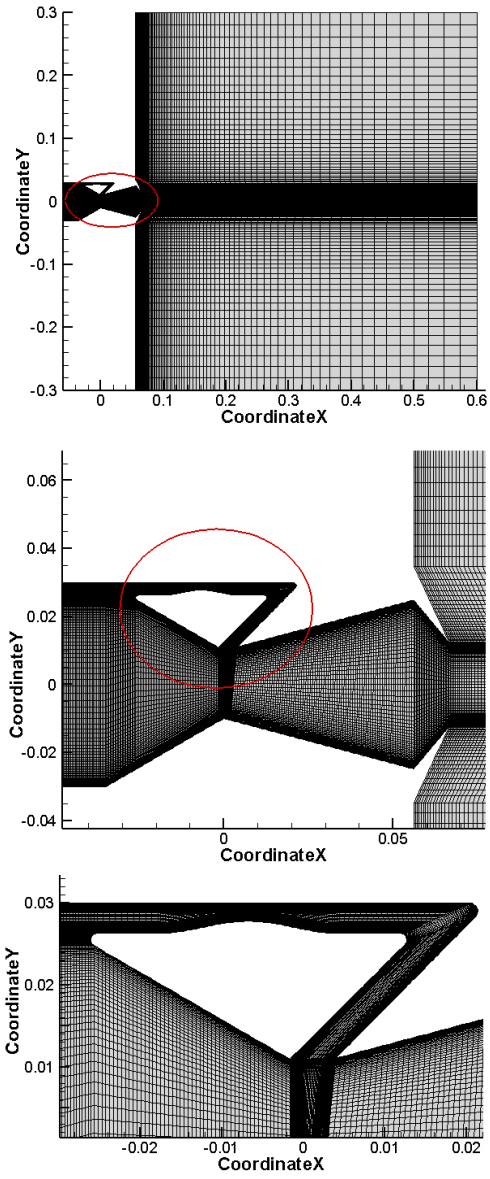

Figure 6. Sketch of the computational grid B with details of the main nozzle and the bypass duct with area contraction

172x390mm (96 x 96 DPI)

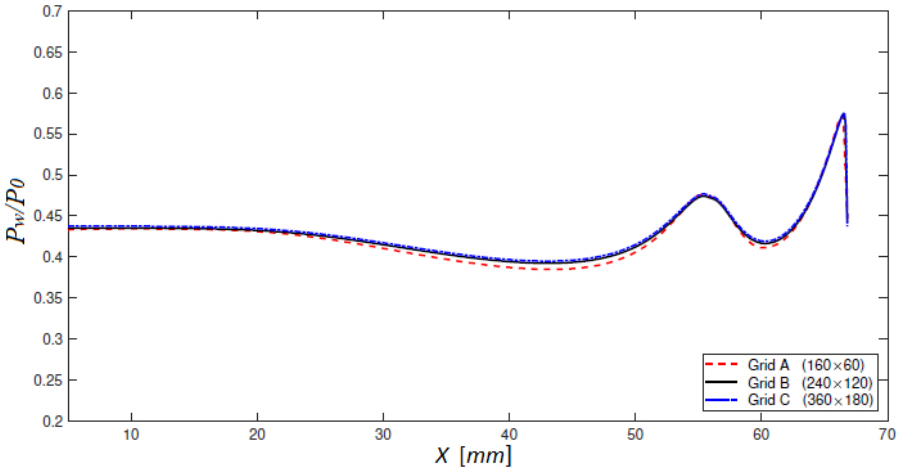

(a) Top wall

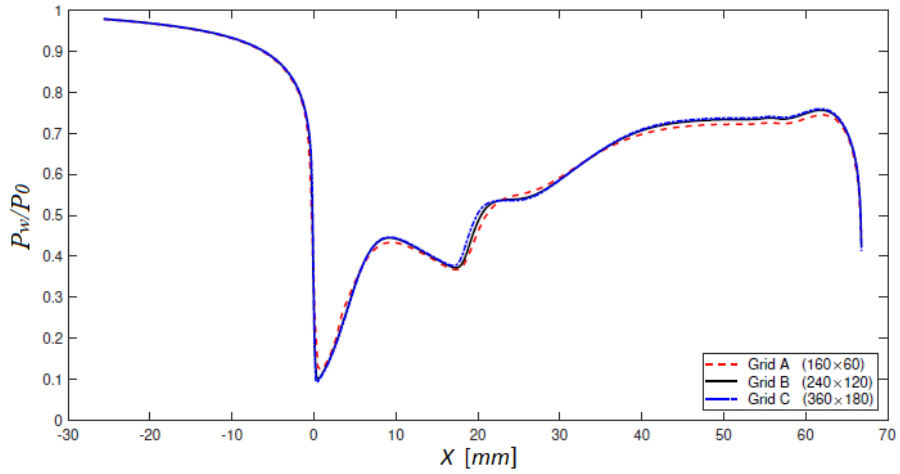

(b) Bottom wall

Figure 7. Computed pressure distributions along the nozzle walls on different grids

199x247mm (96 x 96 DPI)

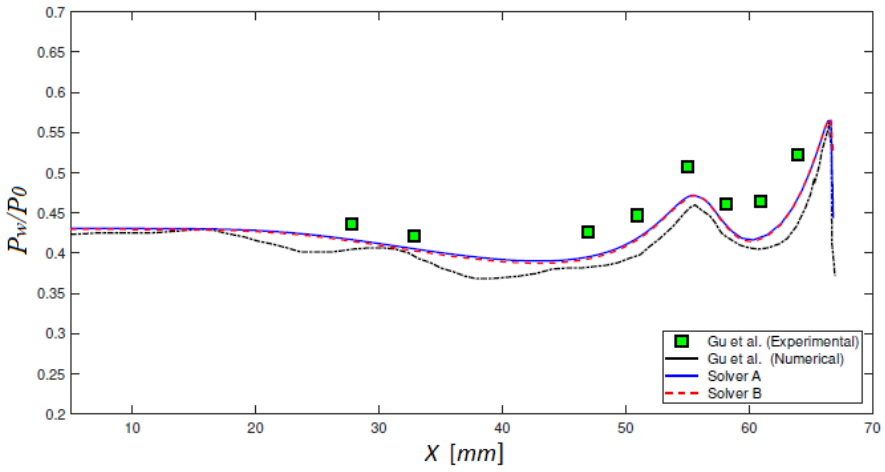

(a) Top wall

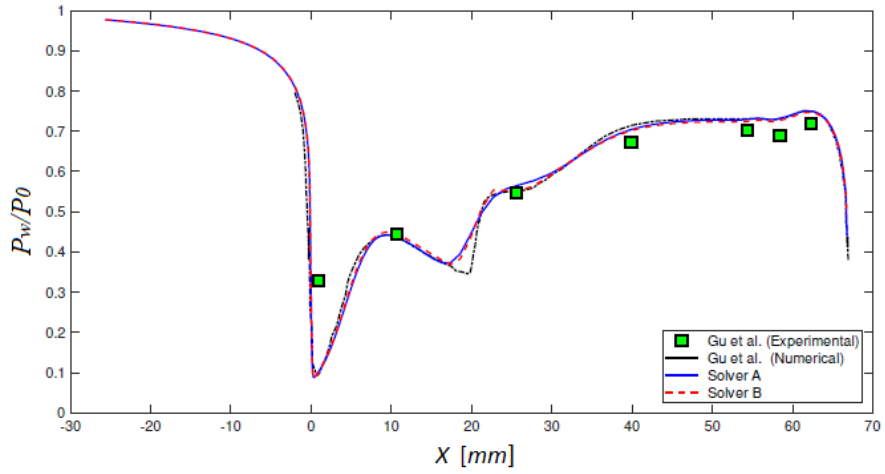

(b) Bottom wall

Figure 8. Pressure distribution along the nozzle walls. Comparison between numerical results and experimental measurements

184x238mm (96 x 96 DPI)

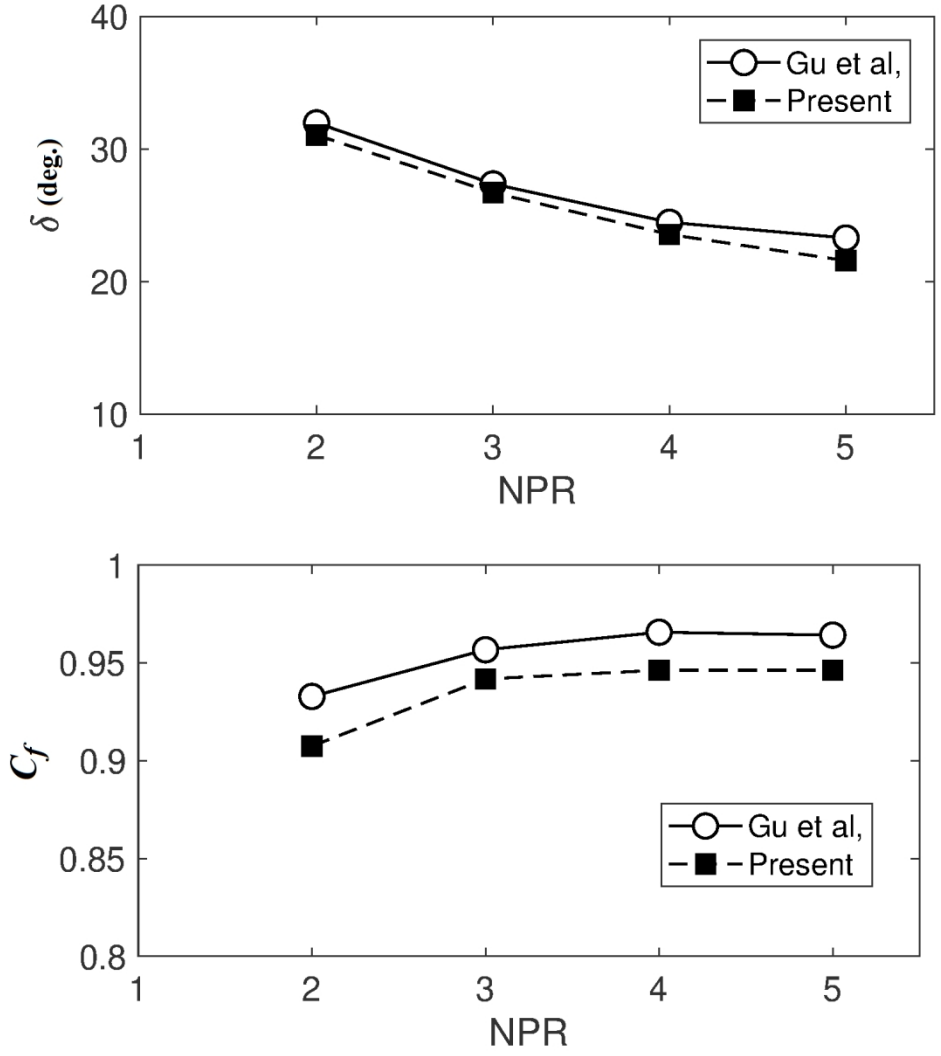

Figure 9. Predicted results of thrust angle δ and system resultant thrust ratio Cf versus nozzle pressure ratio NPR

451x511mm (96 x 96 DPI)

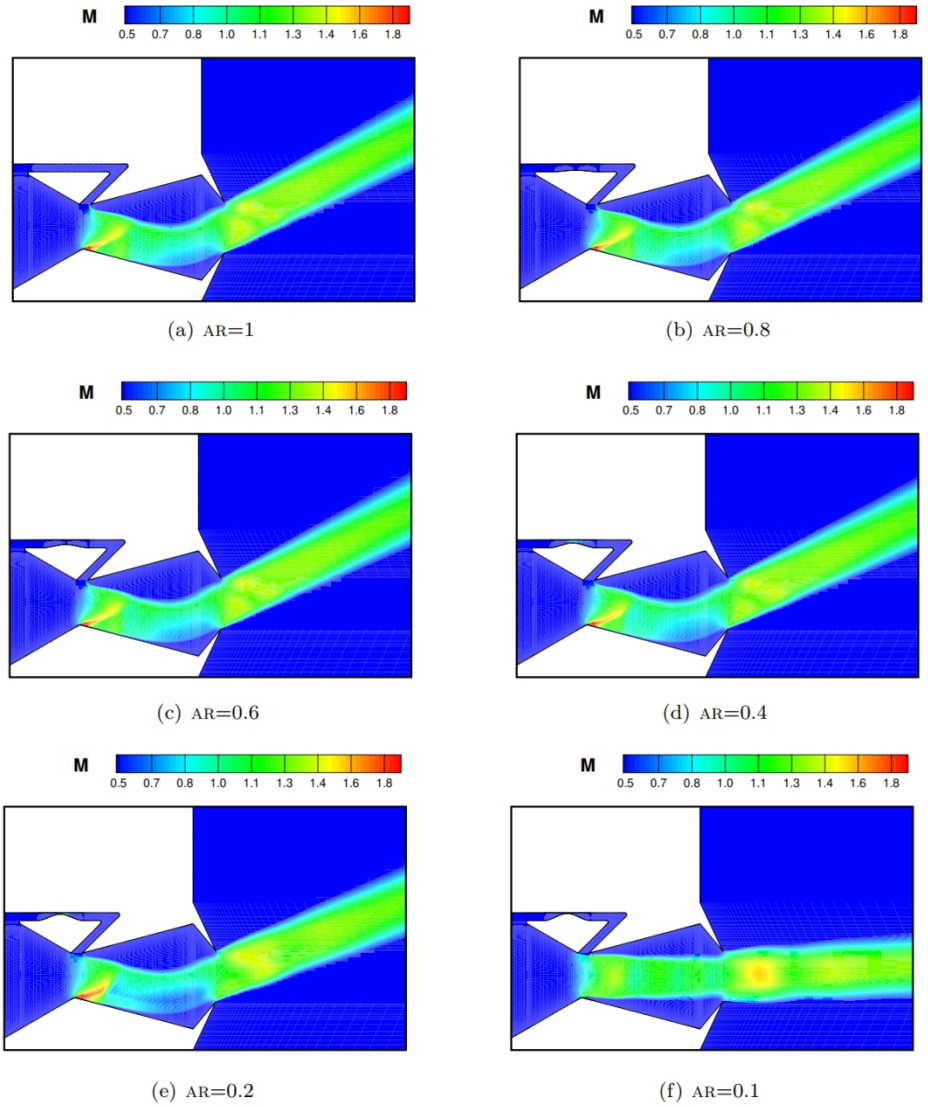

Figure 10. Iso-Mach contour maps of the nozzle flow field for different area contraction ratios AR of the bypass duct

341x389mm (96 x 96 DPI)

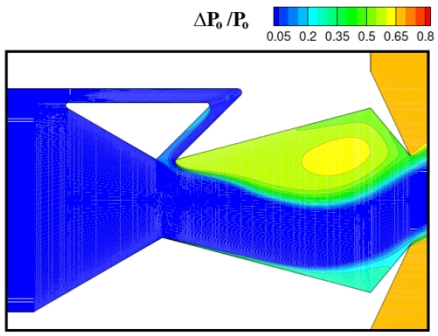

(a) AR = 1

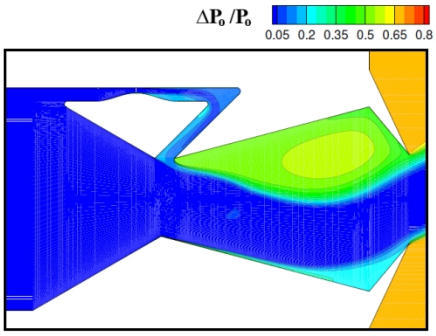

(b) AR = 0.4

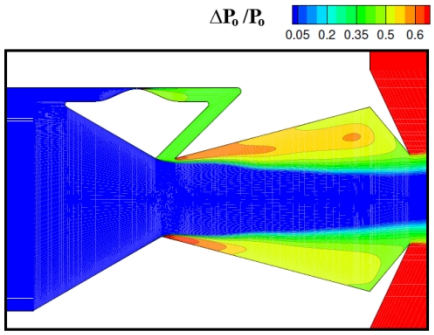

(c) AR = 0.1

Figure 11. Contour maps of the total pressure loss ΔPo/Po for different area contraction ratios AR of the bypass duct. Field values outside the nozzle must be excluded (regions in red)

186x475mm (96 x 96 DPI)

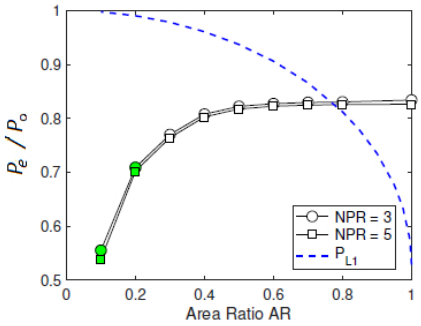

(a)

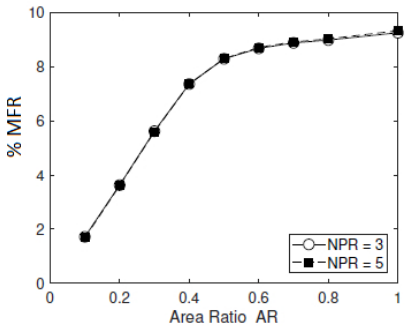

(b)

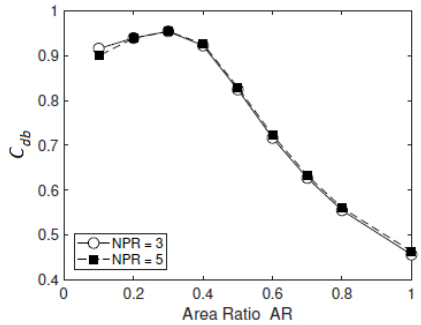

(c)

Figure 12. Averaged static pressure at bypass outlet, mas flow ratio MFR and bypass discharge coefficient Cdb as a function of the area contraction ratio. Green symbols refer to choked bypass conditions

109x275mm (96 x 96 DPI)

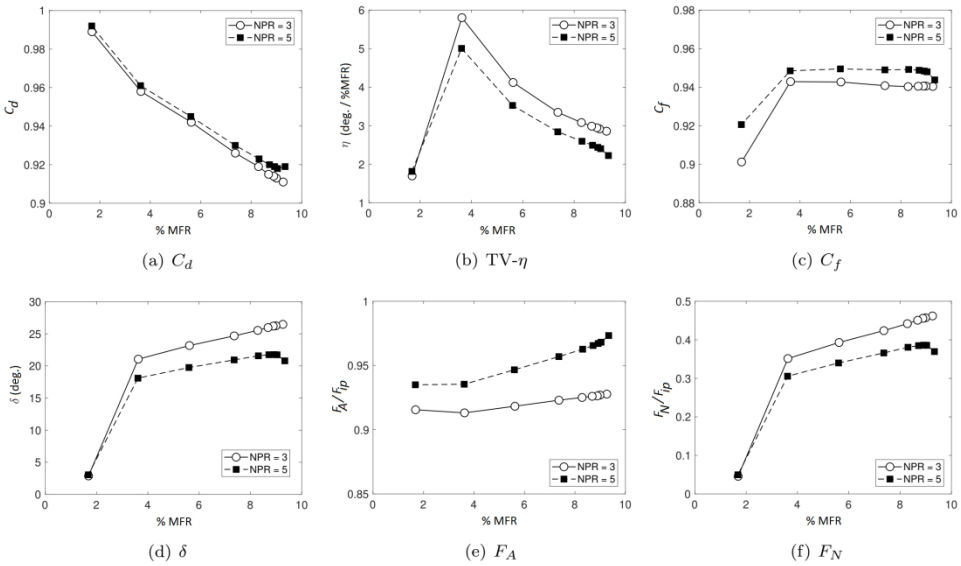

(a) C_d (b) TV-η (c) C_f

(d) δ (e) F_A (f) F_N

Figure 13. Thrust-vectoring performance parameters as a function of the secondary mass flow ratio %MFR

664x391mm (96 x 96 DPI)

Table 1. Bypass dual-throat nozzle dimensions

Parameter	Value
Nozzle throat height H_t	20 mm
Nozzle outlet height H_e	$1.2H_t$
Length of the cavity	$3.34H_t$
Bypass Channel height h_c	$0.185H_t$
Angle θ_1	30º
Angle θ_2	14.8º
Angle θ_3	50º
Angle θ_4	44.8º